Supporting Information: Block copolymer-directed single diamond hybrid structures derived from X-ray nanotomography

Kenza Djeghdi[a], Dmitry Karpov[b,c], S. Narjes Abdollahi[a,d], Karolina Godlewska[a], René Iseli[a], Mirko Holler[b], Claire Donnelly[e], Takeshi Yuasa[f,g], Hiroaki Sai[f,h], Ulrich B. Wiesner[f,i], Ullrich Steiner[a], Bodo D. Wilts[a,j], Michimasa Musya[k], Shunsuke Fukami[k,l,m,n,o], Hideo Ohno[k,l,m,n], Ana Diaz[b], Justin Llandro[k,l], and Ilja Gunkel[a,*]

[a]Adolphe Merkle Institute, University of Fribourg, Chemin des Verdiers 4, 1700 Fribourg, Switzerland

[b]Paul Scherrer Institute, Forschungsstr. 111, 5232 Villigen-PSI, Switzerland

[c]Current affiliation: European Synchrotron Radiation Facility, 71 Av. des Martyrs, 38000 Grenoble, France

[d]Current affiliation: Department of Chemistry, University of Basel, Mattenstr. 24a, BPR-1096, 4058 Basel, Switzerland

[e] Max Planck Institute for Chemical Physics of Solids, Nöthnitzer Str. 40, 01187 Dresden, Germany

[f] Department of Materials Science and Engineering, Cornell University, Ithaca, NY 14853, USA

[g] Current affiliation: Yokkaichi Research Center, JSR Corporation, Yokkaichi, Mie 510-8552, Japan

[h] Current affiliation: Simpson Querrey Institute for Bionanotechnology, Northwestern University, Evanston, IL 60208, USA

[i] Kavli Institute at Cornell for Nanoscale Science, Cornell University, Ithaca, NY 14853, USA

[j] Department for Chemistry and Physics of Materials, University of Salzburg, Jakob-Haringer-Str. 2a, 5020 Salzburg, Austria

[k]Laboratory for Nanoelectronics and Spintronics, Research Institute of Electrical Communication, Tohoku University, 2-1-1 Katahira, Aoba-ku, Sendai 980-8577, Japan

[l] Center for Science and Innovation in Spintronics, Tohoku University, 2-1-1 Katahira, Aoba-ku, Sendai 980-8577, Japan

[m] Center for Innovative Integrated Electronic Systems, Tohoku University, 468-1 Aramaki Aza Aoba, Aoba-ku, Sendai 980-0845 Japan

[n] WPI Advanced Institute for Materials Research, Tohoku University, 2-1-1 Katahira, Aoba-ku, Sendai 980-8577, Japan

[o] Inamori Research Institute for Science, Kyoto 600-8411, Japan.

[*] To whom correspondence should be addressed. E-mail: ilja.gunkel@unifr.ch

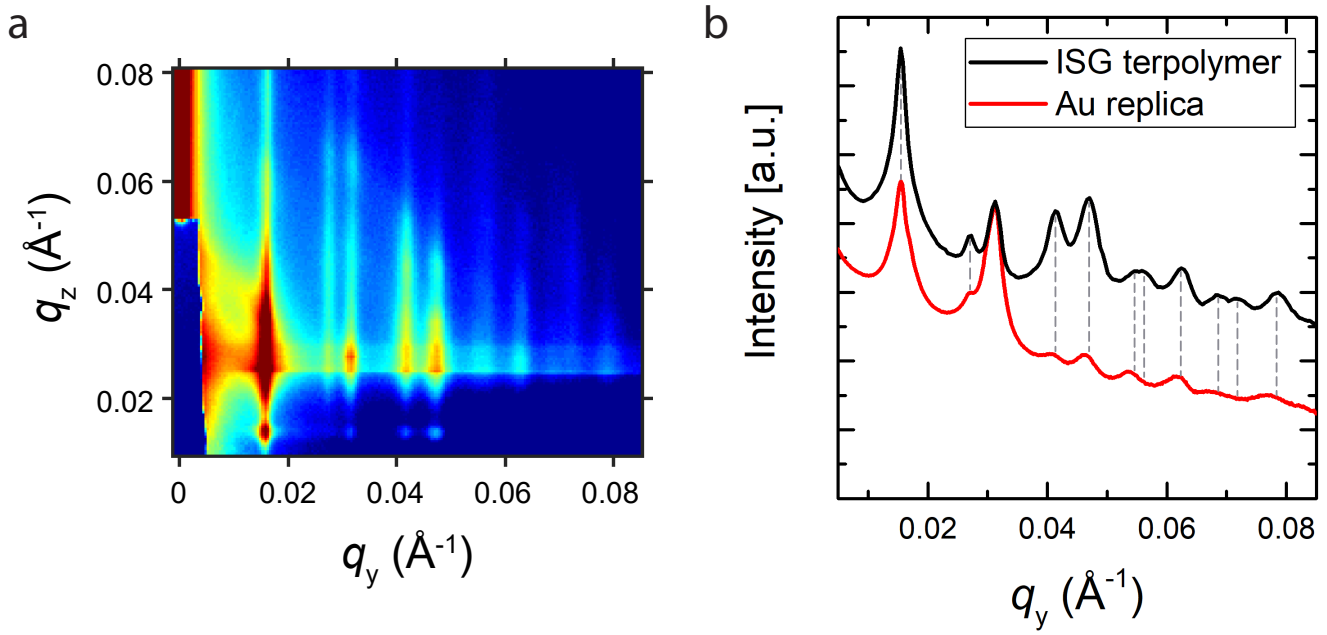

Fig. S1. Small-angle X-ray scattering (SAXS) data from a polymer film and the associated gold replica. a) Grazing-incidence small-angle X-ray scattering (GISAXS) pattern of a solvent-annealed ISG triblock terpolymer film. Note that while the 2D GISAXS pattern features several pronounced peaks in the horizontal direction, thus providing detailed in-plane structural information, the broadened peaks along the vertical axis make it difficult to extract precise quantitative out-of-plane information. b) Horizontal line cut ($q_z = 0.026\,\text{Å}^{-1}$; black line) of the GISAXS pattern shown in (a), and SAXS profile (red line) of a nanostructured gold network replicated from a solvent-annealed ISG template. The first-order peak reflections of both scattering profiles match, and the ratios of the higher-order peaks to the first-order peak also remain consistent (shown by the vertical dashed lines), with slight deviations at larger scattering vectors. See Fig. S12) for the indexing of the gold replica profile. The gold network was prepared from a solvent-annealed ISG template fabricated on FTO-coated glass by electrodeposition. The ISG template was annealed using the same protocol as the sample described in (a). The annealing and replication procedures applied to these samples are identical to those described in the Methods section.

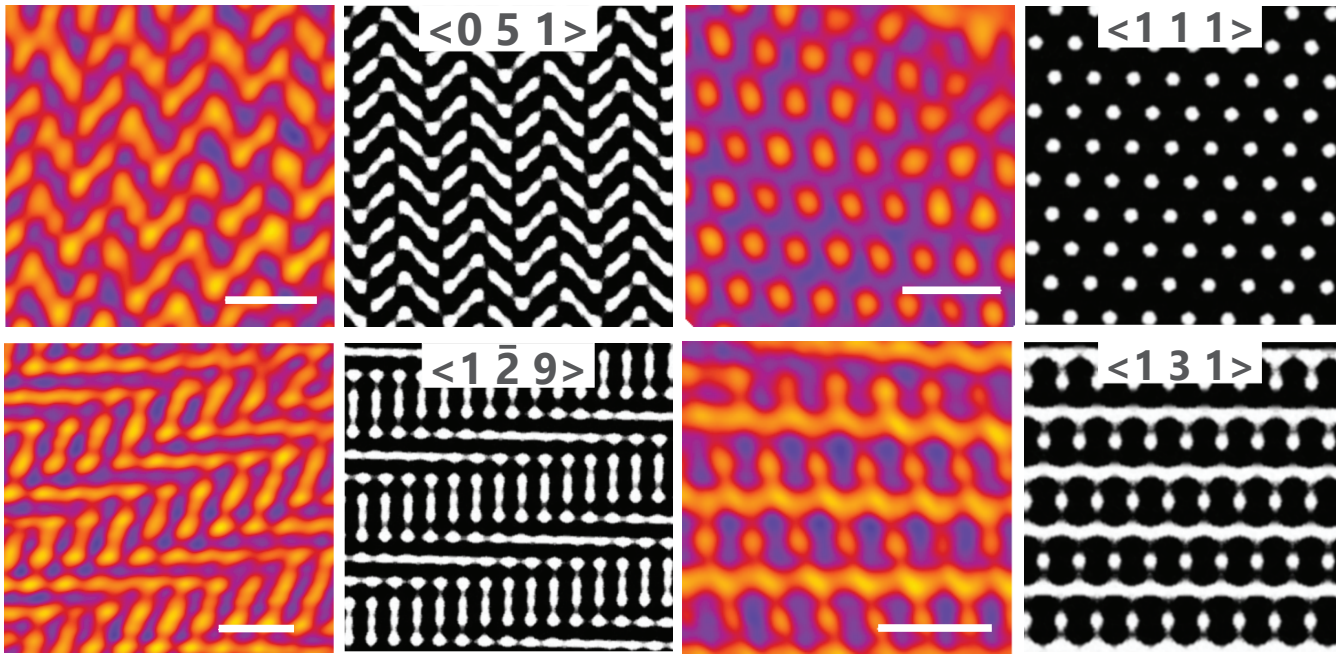

Fig. S2. Additional experimental cross-sectional views. Match between cross-sections extracted from the X-ray tomography dataset (orange-purple colormap) and the $Fd\bar{3}m$ single diamond (SD) level-set (black and white). Miller indices of the SD level-set are written as $\langle \mathrm{hkl} \rangle$. Scale bars: 100 nm.

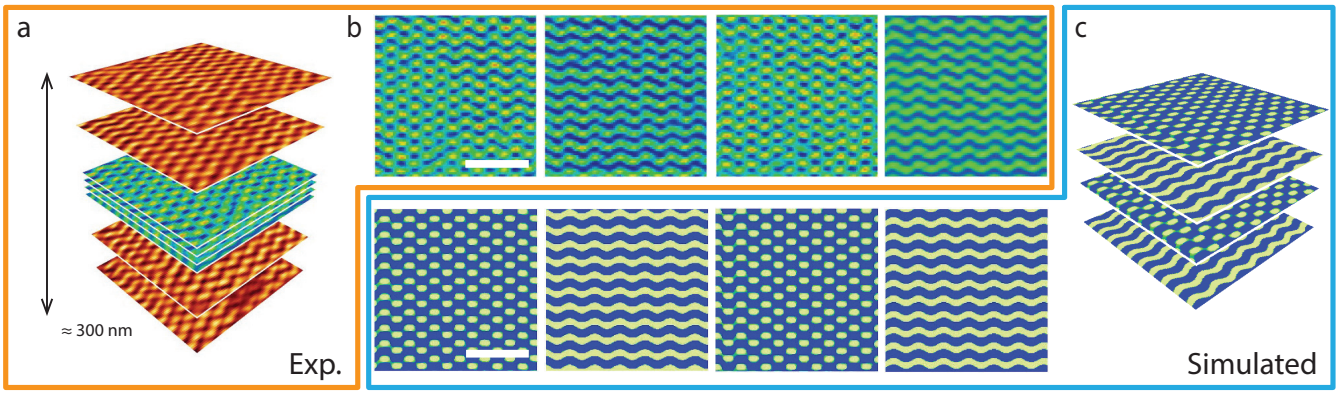

Fig. S3. Experimental and modeled slices parallel to the substrate. a) Experimental slices cut parallel to the substrate over a thickness of 300 nm. The slices alternate between a wavy pattern and stretched hexagons throughout the film. b) Top row: experimental slices shown in a), viewed from top to bottom. The slices are spaced by 12 nm. Bottom row: $\langle 110 \rangle$ oriented slices predicted by the distorted single diamond (DSD) model. Scale bars: 200 nm. c) DSD $\langle 110 \rangle$ slices spaced by 13 nm matching the patterns observed experimentally.

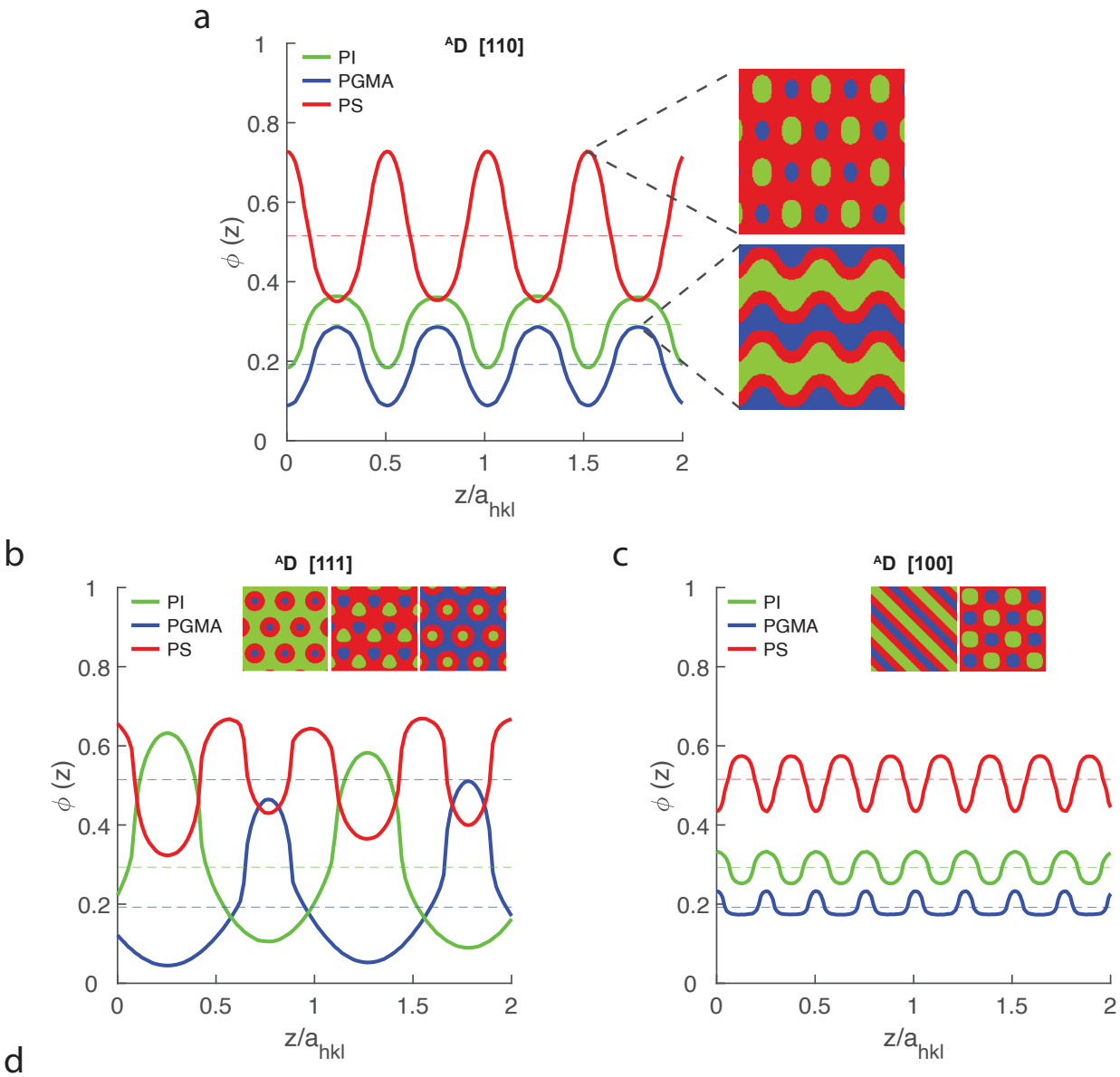

d

^{A}D	avg1	max1	min1	max-min	avg2	max2	min2	max-min	avg3	max3	min3	max-min
110	0.19	0.29	0.09	0.20	0.29	0.36	0.18	0.18	0.52	0.73	0.35	0.38
100	0.19	0.23	0.17	0.06	0.29	0.33	0.25	0.08	0.52	0.57	0.43	0.14
111	0.19	0.51	0.04	0.47	0.29	0.63	0.09	0.54	0.51	0.67	0.32	0.35

^{A}G	avg1	max1	min1	max-min	avg2	max2	min2	max-min	avg3	max3	min3	max-min
110	0.19	0.41	0.07	0.34	0.29	0.55	0.13	0.42	0.51	0.62	0.38	0.24
100	0.19	0.21	0.19	0.02	0.30	0.32	0.27	0.05	0.51	0.54	0.46	0.08
111	0.19	0.25	0.12	0.13	0.30	0.35	0.27	0.08	0.51	0.59	0.45	0.14

Fig. S4. Composition profile of a level-set alternating diamond. Composition profile of each phase of the polymeric structure within two unit cells of an alternating diamond according to the diamond level-set model in eq. 1 for the a) $[110]$, b) $[111]$, c) $[100]$ out-of-plane orientations. The fill fractions of the phases correspond to the composition obtained from the ^{1}H NMR analysis (Fig. S10) and are $f_{\mathrm{PI}} = 0.29$ shown in green, $f_{\mathrm{PGMA}} = 0.19$ shown in blue, and $f_{\mathrm{PS}} = 0.52$ shown in red. The two cross-sections shown represent the maximal and minimal area fraction of the matrix phase (corresponding to the minimal and maximal area fractions of the two other phases). The color of each phase corresponds to the plot lines. d) Area fraction of each phase for various orientations of an ^{A}D and an ^{A}G. For each phase, the average value corresponds to the nominal volume fraction. The maximal and minimal value of the area fraction, as well as their difference, are calculated. The values shown here correspond to the plots in a–c.

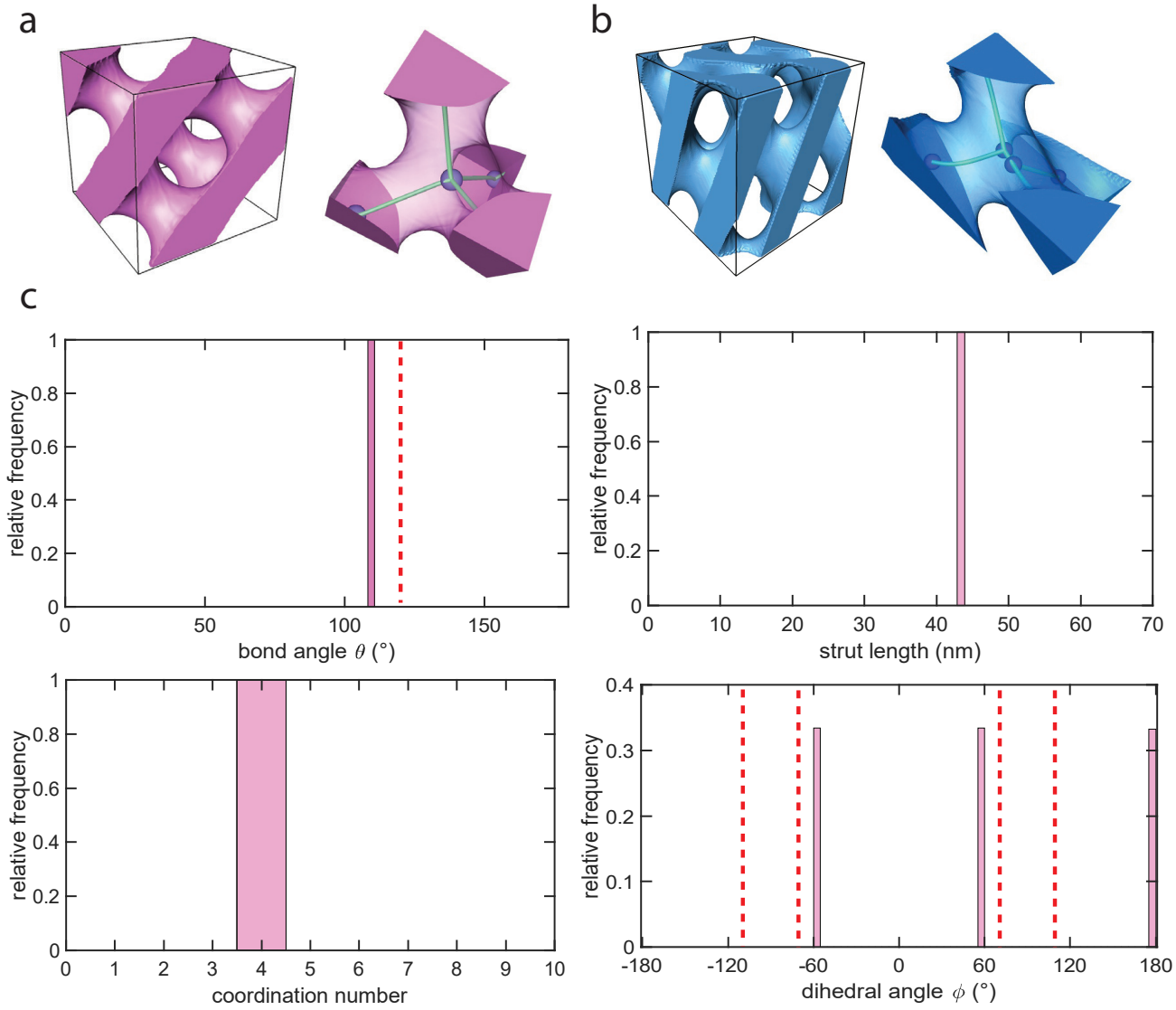

Fig. S5. Cubic diamond and DSD. Views of a) a level-set SD unit cell with $a = 100\,\mathrm{nm}$ and $f = 0.4$ and a single node compared with b) a DSD of same volume and its single strut. c) Statistical analysis of structural parameters of an SD: distributions of bond angle, strut length, coordination number and dihedral angles. The values expected for SD are $\theta = 109.5°$, $\mathrm{CN} = 4$, and $\varphi_d = \pm 60°, \pm 180°$. The values expected for a gyroid ($\theta = 120°$, $\varphi_g = \pm 70.5°, \pm 109.5°$) are shown in red dotted lines as a reference.

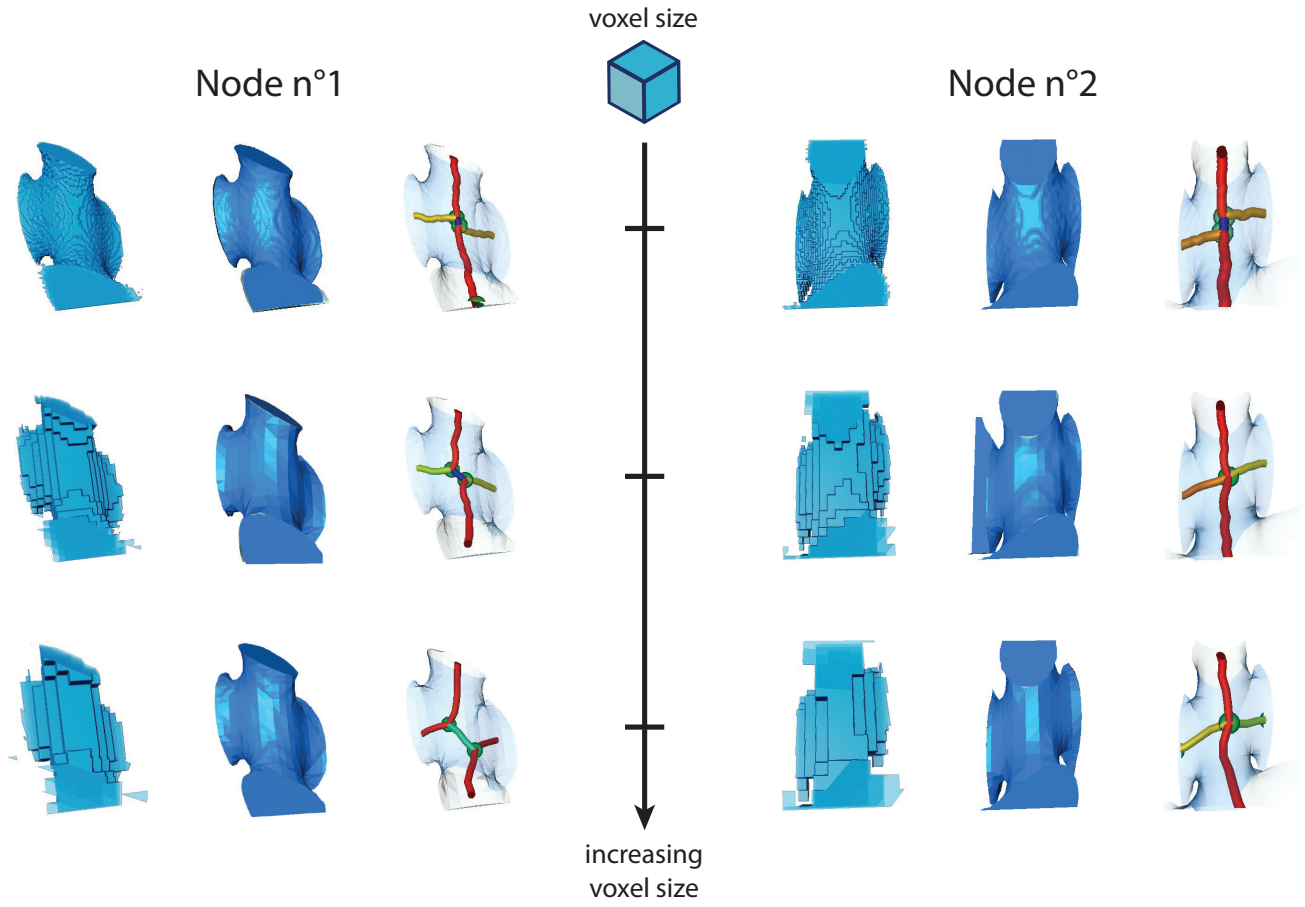

Fig. S6. Voxel size-dependent skeletonization in the DSD. From left to right: voxelized volume rendering, smoothed surface rendering, skeleton. The strut color corresponds to its length, with a blue to red colormap corresponding to the $[5 - 35\,\mathrm{nm}]$ range. Upon decreasing the resolution (i.e. increasing the voxel size), some nodes do not change connectivity (Node n°1), while some have the two nodes linked by the shortest strut merge, thus changing the connectivity from 3 to 4 (Node n°2). This is caused by the dramatic loss of features evident in the voxelized rendering. Voxel size from top to bottom: 0.9 nm, 2.6 nm, 4.3 nm.

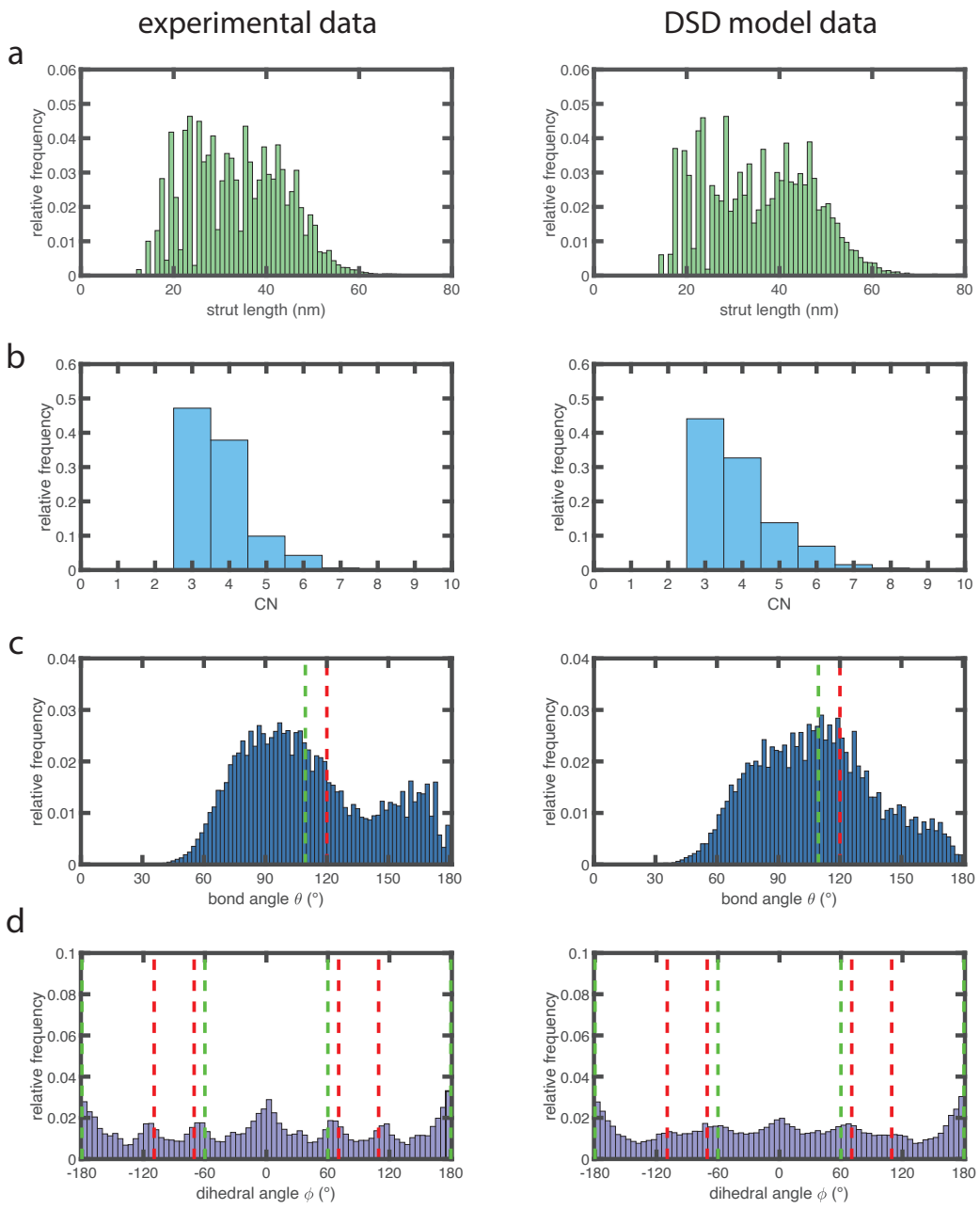

Fig. S7. Comparison of structural parameters statistics calculated on the experimental dataset (left column) and the DSD model (right column). Distribution of the a) strut lengths ($N \approx 20.000$), b) coordination numbers CN ($N \approx 10.000$), c) bond angles θ(°) ($N \approx 60.000$), and d) dihedral angles ϕ(°) ($N \approx 100.000$). The volumes under investigation were $V = 1250 \times 326 \times 1854\,\mathrm{nm}^3$. The voxel size is 6.04 nm in both cases. The angular values expected for a diamond and a gyroid network are shown in green and red dotted lines, respectively.

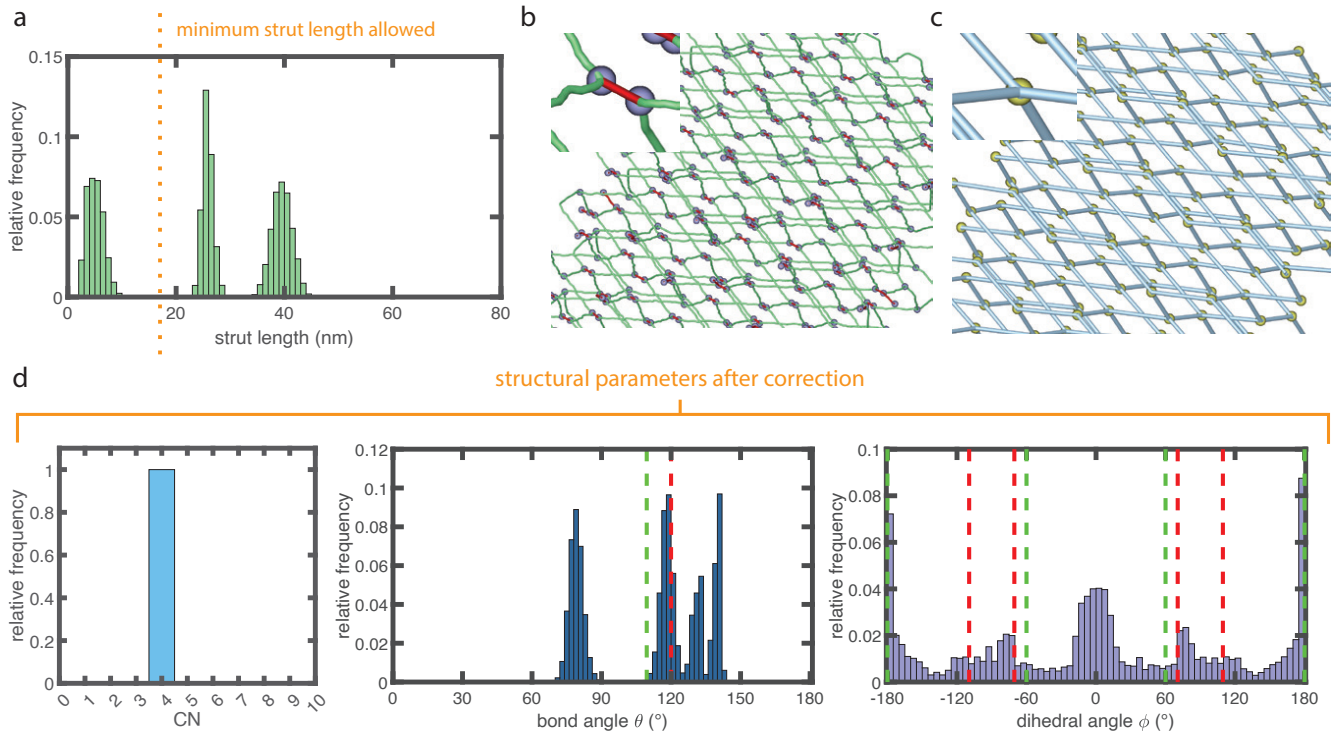

Fig. S8. Structural parameter statistics after upsampling and correcting the skeleton of the DSD model. a) A minimum strut length of 18 nm is imposed in the upsampled DSD model skeleton. Two nodes connected by a strut shorter than 18 nm are merged into one ($N \approx 16.000$). b) DSD model skeleton before correction: the struts smaller than 18 nm are colored in red. The majority of the nodes (purple spheres) appear to be doubled. Inset: magnification of a specific double node. c) Same skeleton after correction. Nodes that were doubled are now merged into a single (yellow) node. The general appearance of the skeleton is otherwise unchanged. Inset: same node as shown in b) after merger resulting from the correction. d) Structural parameters statistics from the corrected DSD model skeleton shown in c). The coordination number ($N \approx 6.000$) is now equal to 4, as expected for a cubic diamond. The deviations of bond ($N \approx 30.000$) and dihedral ($N \approx 25.000$, computed on a smaller subvolume due to computational limitations) angles from the values expected for a cubic diamond (seeFig. S5) reflect the distortions observed in the experimental sample. The values expected for the diamond and gyroid morphologies are shown as references in green and red, respectively. The voxel size is 1 nm.

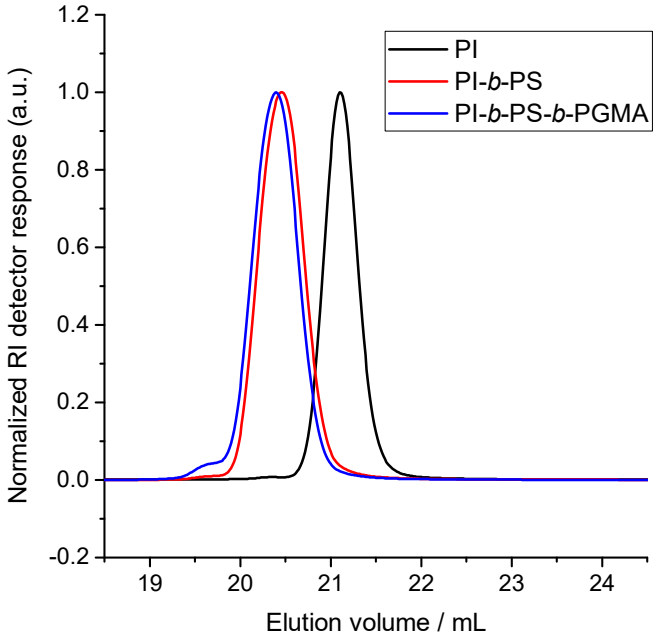

Fig. S9. GPC elugrams of PI homopolymer (black), PI-*b*-PS diblock copolymer (red), and the final PI-*b*-PS-*b*-PGMA (ISG) triblock terpolymer (blue). The GPC was equipped with a Waters 410 refractive index detector and THF was used as the eluent. The elugrams were analyzed against a PI standard curve to deduce the number-averaged molar mass.

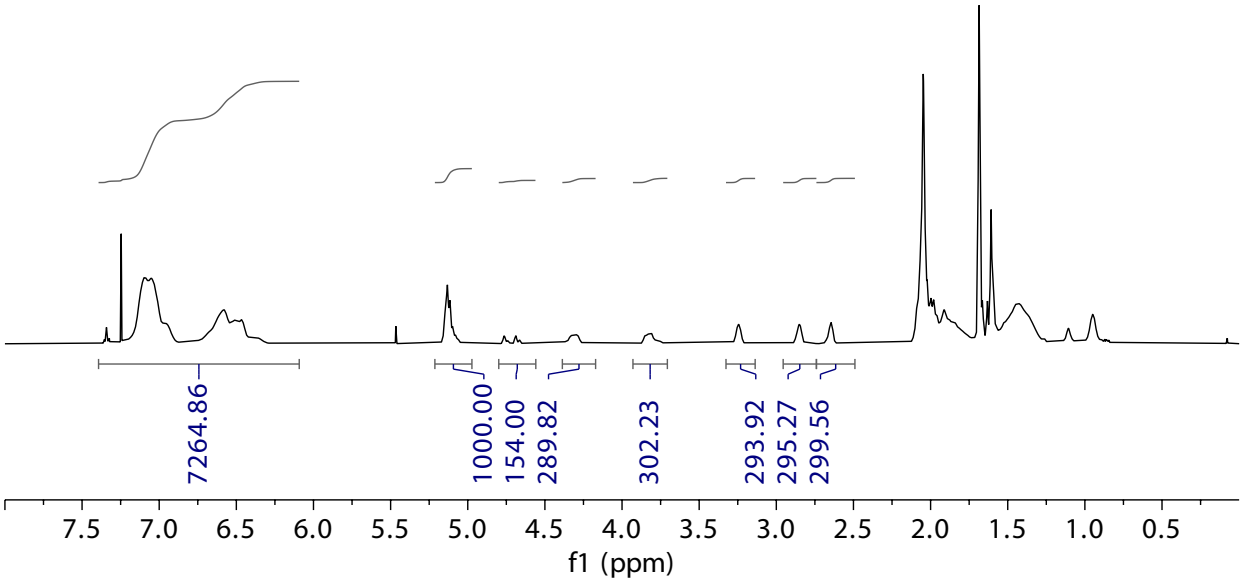

Fig. S10. ^{1}H NMR spectrum of the ISG triblock terpolymer collected on a Varian Mercury-300 or Inova-400 spectrometer using chloroform-d as the solvent.

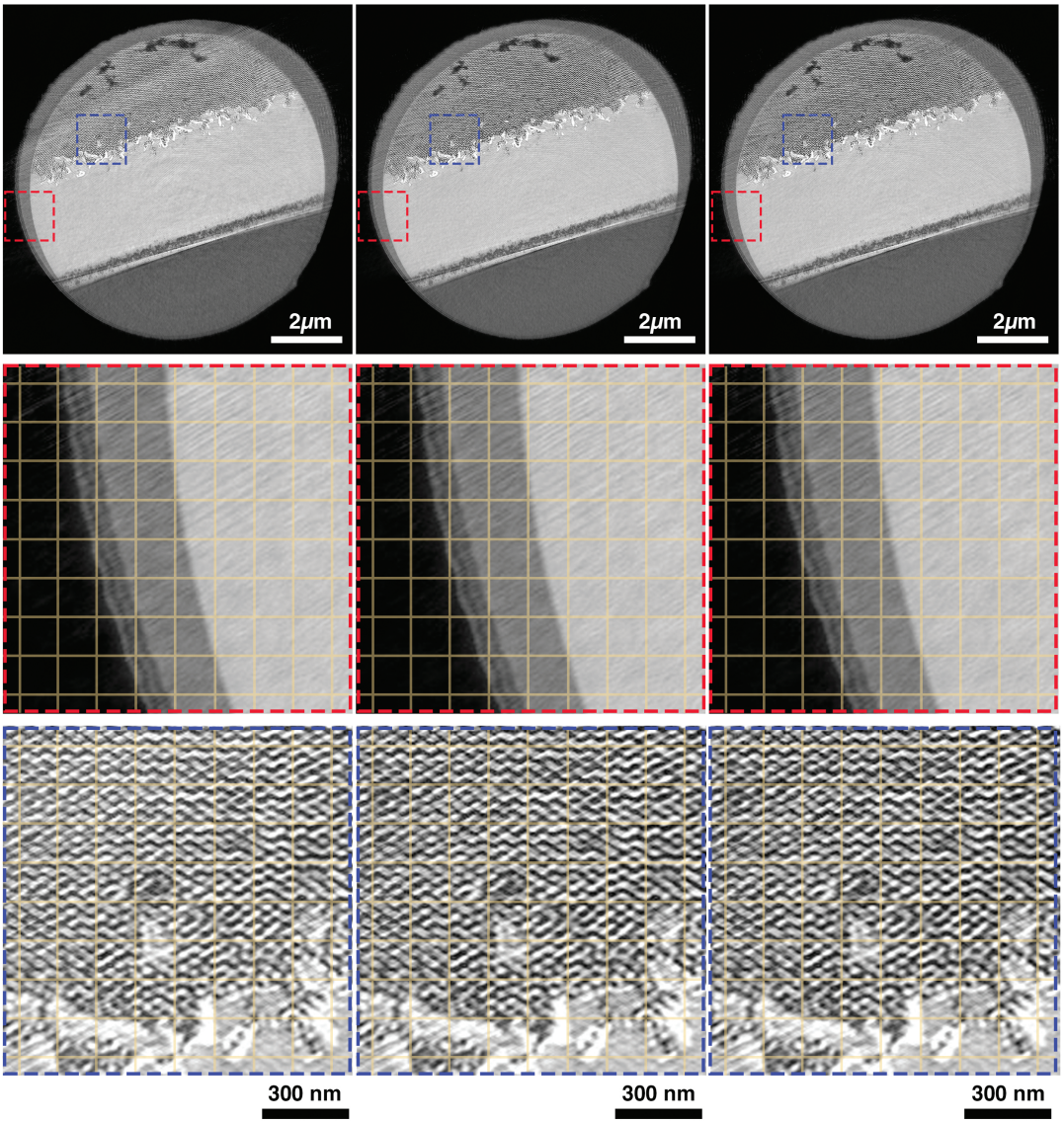

Fig. S11. Sub-tomograms. *Top*: Slices through the 1st (left), 5th (center), and 8th (right) subtomogram. *Middle*: Zoomed-in region marked with a red square in the corresponding top slice. *Bottom*: Zoomed-in region marked with a blue square in the corresponding top slice. The semi-transparent grid is added to assist visual comparison of the structures.

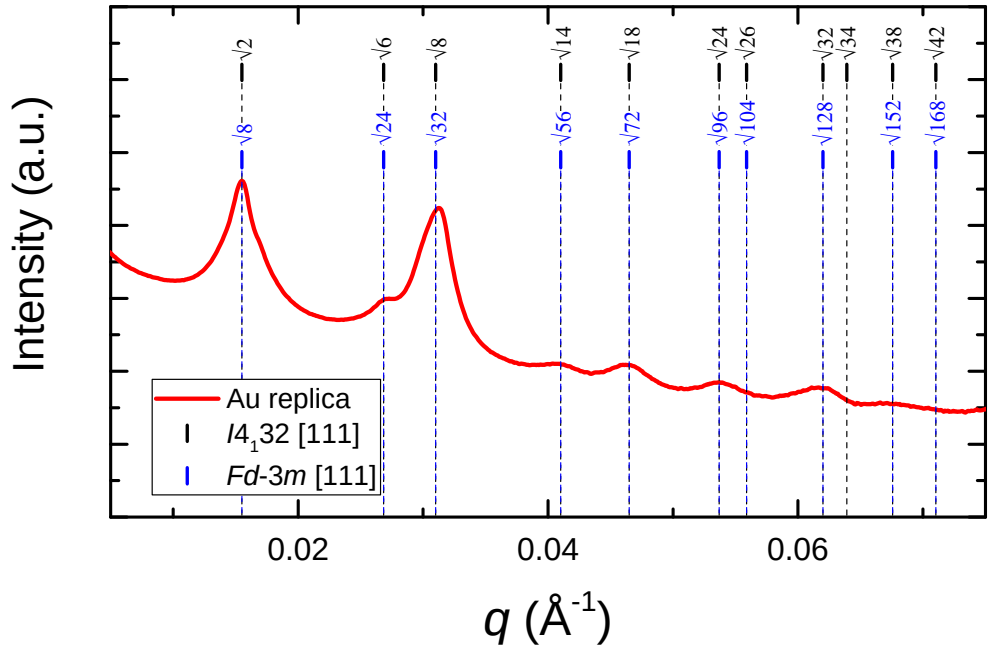

Fig. S12. Azimuthally averaged SAXS curves of gold replica. The gold nanostructures were replicated from a solvent-annealed ISG template prepared on FTO-coated glass by electrodeposition. The sample was annealed and replicated into gold according to the protocol described in the Methods section. The profile was indexed with the expected peak positions for the $I4_132$ (single gyroid; black vertical bars) and $Fd\bar{3}m$ (single diamond; blue vertical bars) space groups, with the $[111]$ direction perpendicular to the substrate. The first eight reflections of these two peak sequences coincide, making the structural assignment ambiguous as the distinguishing higher-order peaks are less intense and broader than those common to both structures. Assuming a $[111]$ orientation, the first-order peak at $q = 0.155\,\mathrm{nm}^{-1}$ corresponds to the $\sqrt{2}$ reflection for $I4_132$ and $\sqrt{8}$ reflection for $Fd\bar{3}m$, giving lattice parameters of $\langle a\rangle = 2\pi\sqrt{2}/q = 70\,\mathrm{nm}$ ($I4_132$) and $\langle a\rangle = 2\pi\sqrt{8}/q = 115\,\mathrm{nm}$ ($Fd\bar{3}m$). Importantly, these average lattice parameters $\langle a\rangle$ do not capture the lattice distortions with unit cell parameters of $a = 75\,\mathrm{nm}$, $b = 108\,\mathrm{nm}$, and $c = 49\,\mathrm{nm}$ quantified by X-ray nanotomography analysis (Figure 3b).